Journal of Materials Chemistry C

ROYAL SOCIETY OF CHEMISTRY

PAPER

View Article Online
View Journal | View Issue



Cite this: J. Mater. Chem. C, 2020, 8, 262

# Electric-field enhancement of molecularly imprinted sol–gel-coated Au nano-urchin sensors for vapor detection of plant biomarkers†

Bin Chen, *[ab] Chuanjun Liu,[b] Liang Shang,[b] Hao Guo,[b] Jiongming Qin,[a] Lingpu Ge,[b] Chun Ju Jing,[a] Changhao Feng[a] and Kenshi Hayashi *[b]

Received 9th October 2019,
Accepted 18th November 2019

DOI: 10.1039/c9tc05522c

rsc.li/materials-c

Detection of plant volatile organic compounds (VOCs) provides a new approach for real-time, on-field crop growth monitoring in agriculture. Gold (Au) nano-urchins with branched tips were synthesized and deposited on glass slides with controlled densities to generate enhanced electronic hot spots. The refractive index (RI) sensing capability of the slides was investigated as a function of nano-urchin density. A molecularly imprinted sol–gel (MISG) solution was spin-coated on the slide having the optimum RI sensing capability to form the MISG@Au nano-urchin sensors. Four MISGs were developed for the detection of typical plant biomarker VOCs: *cis*-jasmone, limonene, α-pinene, and γ-terpinene. The normalized response indicated that selectivity of the MISG@Au nano-urchin sensors to the corresponding template terpenes was generated. According to the principal component analysis (PCA), both of the peaks in the absorption spectrum took necessary effects on terpene detection and discrimination, which was attributed to the hot spots generated by the Au nano-urchins and their coupling effects.



## 1. Introduction

Volatile organic compounds (VOCs) emitted by plants in metabolic processes have many complex functions, such as herbivore deterrence,[1,2] attraction of species-specific pollinators,[3] and disease warning.[4,5] Methyl salicylate is an efficient repellent for migrating aphids.[6] Thaler *et al.* have reported that a boost of signal transduction could be realized *via* manipulating salicylic acid and jasmonic acid plant hormones, and that the enhanced release of VOCs in crops might improve biological control.[7] An increase in isoprene, monoterpene and sesquiterpene emission from pine trees has been attributed to high-temperature stress.[8–10] Lofeto *et al.* reported that the emission of isoprenoids from Italian vegetation is a self-protection signal against oxidative stress.[3] The quantitative and qualitative compositions of plant VOCs such as *cis*-jasmone, limonene, α-pinene, γ-terpinene are important for growth or disease-status diagnoses.[8,11–13] Hence, high-precision on-field discrimination and detection of plant biomarker VOCs are critically important.

Instrumental vapor analysis methods such as gas chromatography,[14] mass spectrometry,[15] and infrared detection[16] have high-precision and specification. In gas chromatography, a sample vapor is transported in a column by a carrier gas, with a retention time that is a function of the chemical and physical properties. A detector is then used to monitor and detect the vapor by the retention time and quantity. These analysis methods can be complex, costly, and time-consuming. Most common gas sensors use piezoelectric[17,18] or metal oxide materials.[19,20] Piezoelectric sensors could be divided into surface acoustic wave and quartz-crystal microbalance sensors, both of which have a frequency dependence on the vapor concentration. The performance of these sensors can be affected by surrounding interferences. Metal-oxide sensors detect vapors *via* the conductance that is proportional to vapor concentration. Usually, a high temperature of 200–500 °C at the back sensor is necessary to prompt the interaction between the metal oxide and the vapor molecules.

Localized surface plasmon resonance (LSPR) is due to the confinement of surface plasmon at the nanoscale.[21] Based on LSPR, nanoparticles (NPs) of gold (Au), silver, platinum, and their alloys are extremely sensitive to refractive index (RI) changes, and they have been used as chemical sensors,[22,23] biosensors,[24–26] or gas sensors.[27,28] However, without surface modification, these noble-metal NPs lack selectivity. Hence, a combination of materials having selective adsorption

[a] Chongqing Key Laboratory of Non-linear Circuit and Intelligent Information Processing, College of Electronic and Information Engineering, Southwest University, Chongqing 400715, China. E-mail: chenbin121@swu.edu.cn
[b] Department of Electronics, Graduate School of Information Science and Electrical Engineering, Kyushu University, Fukuoka 819-0395, Japan

† Electronic supplementary information (ESI) available. See DOI: 10.1039/c9tc05522c

capabilities and NPs is needed. For example, sol–gels are polymers with good rigidity, as well as chemical and thermal stability.[29,30] In addition, they are easy to prepare *via* hydrolysis and polycondensation processes without high temperatures.[31] In the sol–gel process, template molecules can interact with the monomer *via* hydrogen bonds, π–π bonds, or van der Waals forces.[32] After removing the template molecules from the sol–gel, cavities with shapes similar to those of templates are left in the matrix. Previous work revealed that a molecularly imprinted sol–gel (MISG) coated on Au NPs exhibited good selectivity to *cis*-jasmine vapor.[32]

Here, branched Au nano-urchins were synthesized and deposited on glass slides. Both theoretical calculations and experimental results indicated large electromagnetic field enhancements at the tips of the branched NPs, which was significant for RI sensing.[33] In addition, the distance between NPs greatly affected the electric field coupling, which generated electronic hot spots that increased the RI sensitivity. Two peaks in the UV-vis spectra of Au nano-urchin films were measured, and the second peak was mainly ascribed to the coupling effect among nano-urchins. A MISG mixture was spin-coated on nano-urchins deposited on the glass slides; 6 μL of MISG spin-coated at 1000 rpm was found to be optimum for RI sensing. Four separate MISG@Au nano-urchins sensors were developed for *cis*-jasmine, limonene, α-pinene, and γ-terpinene detection. The sensor performances were found to be sensitive and selective to the corresponding terpenes. Using principal component analysis (PCA), the four terpene vapors were separated into four clusters.

# 2. Experimental

## 2.1 Chemicals and materials

Titanium tetrabutoxide (TBOT), isopropanol, *cis*-jasmone, limonene, γ-terpinene, titanium tetrachloride ($TiCl_4$), acetone, trisodium citrate, hydroquiene, and ethanol were purchased from Wako Pure Chemical Industries Co., Ltd (Osaka, Japan). (3-aminopropyl)triethoxysilane (APTES) was purchased from Shin-Etsu Chemical Co., Ltd (Tokyo, Japan). $HAuCl_4{\cdot}3H_2O$ and α-pinene were purchased from Sigma-Aldrich (St. Louis, MO, USA). All reagents were used as received.

## 2.2 Instrumentation

Scanning electron microscopy (SEM, SU8000, Hitachi, Japan) was used to image sensor morphologies. The absorbance spectra were recorded using a UV-vis spectrophotometer (UV1800, Shimadzu, Japan) for spectral calibration. The optical sensing system included a tungsten-halogen light source (LS-1, Ocean Optics, USA), a sensing cell, and a UV-vis spectrometer (HR4000 Ocean Optics, USA), with OPwave+ software (Ocean Optics, USA). A spin-coater (MS-B100, Opticoat, Japan) was utilized to make MISG films. PCA analysis was performed with R (version 3.4.3). FDTD simulations were performed using a commercial simulation program (FDTD solutions 8.11.422 by Lumerical Solutions). In the simulation, a total-field scattered-field light source with a wavelength of 400–900 nm was propagated along the *z*-axis and perpendicular to the *x*–*y* plane of the Au nano-urchins and a perfectly matched layer was involved in all boundary conditions. The override mesh cell size used was $1 \times 1 \times 1$ nm$^3$.

## 2.3 Synthesis of Au nano-urchins

Au nano-urchins were synthesized according to a previously reported method, with certain modifications.[34,35] The first step was to synthesize spherical gold seeds *via* citrate reduction; 75 mL of a 100 mM $HAuCl_4$ aqueous solution was added to 30 mL of deionized water in a flask that was vigorously stirred and heated until boiling. Then, 900 mL of 1 w/v% trisodium citrate aqueous solution was added and the mixture was kept boiling until its colour became wine red. The seed solution was cooled to room temperature with stirring. The second step was to grow the Au nano-urchins by placing 25 μL of 100 mM aqueous $HAuCl_4$ into 9.6 mL of deionized water with vigorous stirring. The prepared seed solution (150 μL, 200 μL, 250 μL, and 300 μL), 22 μL of 1 w/v% trisodium citrate aqueous solution, and 1000 μL (or 1200 μL) of 30 mM hydroquinone were added sequentially and stirred for another 30 min. The amounts of seed and hydroquinone solutions were optimized to obtain Au nano-urchins with approximately 60 nm diameter branched tips.

## 2.4 Preparation of MISG solutions

MISG solutions were prepared as previously reported.[36] TBOT (135 μL) was dissolved in 2 mL of isopropanol. 50 μL of template solutions of *cis*-jasmone, limonene, α-pinene, or γ-terpinene templates and 50 μL of APTES were sequentially added with stirring. Then, 25 μL of $TiCl_4$ was added to initiate the MISG solution, after which the MISG solution was pre-hydrolysed in a water bath at 60 °C for 1 h with stirring. The mixture was then vigorously stirred for 8 h at room temperature before spin coating.

## 2.5 Fabrication of MISG@Au nano-urchin sensors

Au nano-urchin slides were fabricated as follows: pre-cleaned glass substrates were immersed in a (1 : 20) volume ratio of an APTES/ethanol solution for 2 h, and then thoroughly washed with ethanol and dried in a nitrogen stream. The surface modified substrates were tiled at the bottom of a glass dish. By controlling the volume or density of the prepared Au nano-urchin solutions, slides with various well-defined densities of nano-urchins were prepared. The MISG template-mixture was then spin-coated onto the slide and heated at 60 °C for 8 h to complete MISG fabrication and template evaporation. Samples were stored under vacuum for 24 h before spectral analysis.

## 2.6 Vapor generation and detection platform

The plant biomarker terpene vapor generation used a headspace method that was previously reported.[26,36] A 6 mL glass bottle with 2 mL of terpene liquid was equipped with a LabView gas flow controller (2014, National Instruments, Austin, USA). The terpene vapor concentrations (ppm) were calculated by:

$$C = k \times D_r \times 10^3/F \quad (1)$$

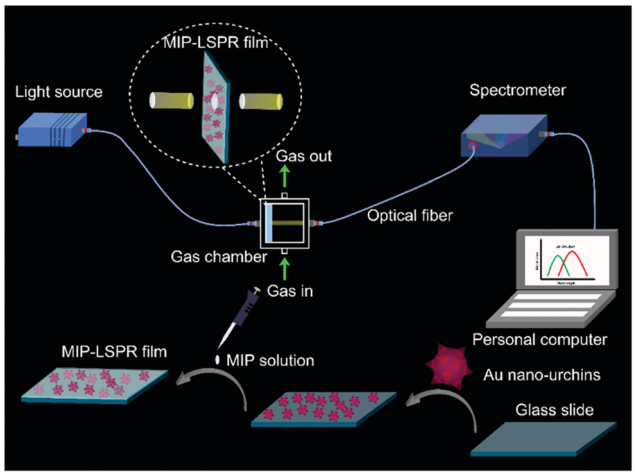


Fig. 1 Schematic of sensor fabrication and terpene vapor detection.

where $D_r$ was the diffusion rate (μg $min^{-1}$), $F$ was the flow rate of the dilute air (L $min^{-1}$), and $k$ was the factor used to convert vapor weight to volume, calculated by:

$$k = 22.4/M \times (273 + t)/273 \times 760/P \quad (2)$$

$M$ was the molecular weight of the terpene molecule, $t$ was the temperature in the gas chamber (25 °C), and $P$ was the gas pressure (760 mmHg). The optical sensing system is shown in Fig. 1. Vapor responses were recorded for a 600 s vapor flow followed by a 600 s air flow. The calculated concentrations of the target terpene vapors were 10 ± 1 ppm *cis*-jasmone, 971 ± 59 ppm limonene, 750 ± 36 ppm γ-terpinene, and 188 ± 34 ppm α-pinene under a flow rate of 0.5 L $min^{-1}$.

# 3. Results and discussion

## 3.1 UV-vis spectra of the Au nano-urchin solution

The Au nano-urchin solution was prepared in water, and both trisodium citrate and hydroquinone served as reductants. The diameter of the Au nano-urchins was controlled to be at approximately 60 nm to make sure that the LSPR can fall in the UV-vis region. According to Yang *et al.*, the diameter and branches of the nano-urchins were more easily tuned by separately controlling the gold seed and hydroquinone concentration.[34] $HAuCl_4$ is reduced from $Au^{III}$ to $Au^{I}$ by citrate, and further reduced to $Au^0$ by hydroquinone. When the amount of $HAuCl_4$ is fixed, addition of a few seeds led to a higher $Au^0$/seed ratio, providing more $Au^0$ to supply the growth of each NP. As a result, the formation of bigger NPs was favoured. On the other aspect, a higher $Au^0$/seed ratio facilitated a branched growth rather than an isotropic one, which also depended on the amount of hydroquinone. A high concentration of hydroquinone with excess $Au^0$ on the seed surface promotes the rapid deposition of $Au^0$, resulting in branched growth. As shown in Fig. S1(a–d) (ESI†), when the amount of gold seed increased from 150 μL to 300 μL, with the amount of $HAuCl_4$, sodium citrate, and hydroquinone fixed at 25 μL, 22 μL, and 1000 μL, respectively, the colour of the solutions changed from blue-pink to pink, and the absorption spectra blue-shifted. Branches were being lost with the increase of gold seed, see Fig. S2(a–d) (ESI†). It was found that 150 μL of gold seed kept the branched structure. In addition, the amount of hydroquinone was further increased from 1000 μL to 1200 μL, with the amount of $HAuCl_4$ and sodium citrate respectively fixed at 25 μL and 22 μL, and the amount of seed was increased from 150 μL to 300 μL. Similar spectral and morphological variations were observed. A slight right shift in the spectrum with increased hydroquinone addition was observed. Hence, the synthesis using 25 μL of $HAuCl_4$, 22 μL of sodium citrate, 150 μL of gold seed, and 1200 μL of hydroquinone was found to be optimum for preparing branch-tipped nano-urchins. TEM images of Au nano-urchins formed under the optimal conditions are shown in Fig. 2.

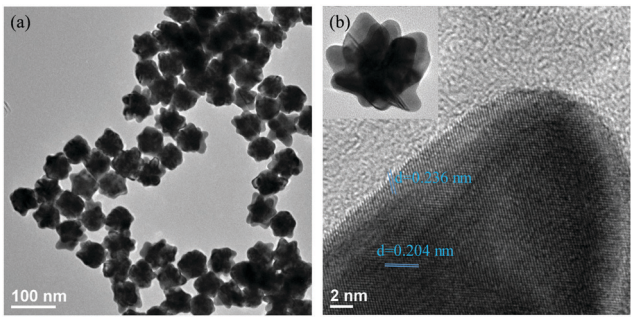


Fig. 2 (a) TEM images of Au nano-urchins and (b) HRTEM image of one branch of a Au nano-urchin.

## 3.2 Optical characteristics of glass slides with deposited Au nano-urchins at various densities

Optimized Au nano-urchins were deposited on glass slides and the spectral characteristics were affected by the sizes, shapes, the effective RI of the surrounding, and the neighbouring distances (Qiu and Wei, 2014).[37] The distance between NPs had a great effect on the electric field coupling, which generated extremely enhanced local electromagnetic fields, or "hot spots" (Jain *et al.*, 2007).[38] Hence, the deposition density of the Au nano-urchins on the glass slides was controlled by changing the volume and concentration of the Au nano-urchin solution. As illustrated in Fig. 3(a), when the deposition density increased, a second absorption peak appeared in the range of 700–1000 nm. The first spectral peak was attributed to the LSPR dipole polarization from single nano-urchins, while the second peak was attributed to coupling effects among nano-urchins.[39–41] The density increase was confirmed by SEM images shown in Fig. 3b–g. The intensity of the first peak also increased with the deposition density, and the colour of the glass slides changed from light pink to dark blue. The different deposition densities were numbered 1 to 6.

To investigate the RI sensing capability of the numbered glass slides, the RI was changed from air to water. As shown in Fig. 4, there were four response parameters used to evaluate the RI response performance: $\Delta A_1(A - A_1)$, $\Delta\lambda_1(\lambda - \lambda_1)$, $\Delta A_2(A - A_2)$, and $\Delta\lambda_2(\lambda - \lambda_2)$. The wavelengths $\lambda_1$ and $\lambda_2$ represented the first

 

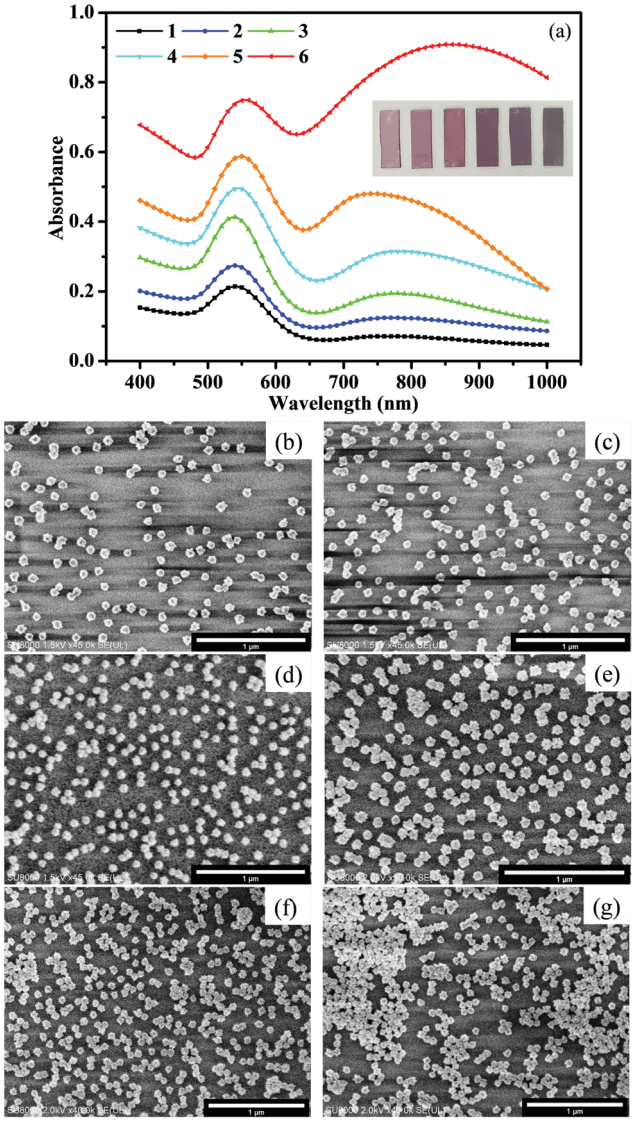


Fig. 3 (a) Absorption spectra of various densities of Au nano-urchins on glass slides, (b–g) SEM images of slides with various Au nano-urchin densities (number 1 to 6).

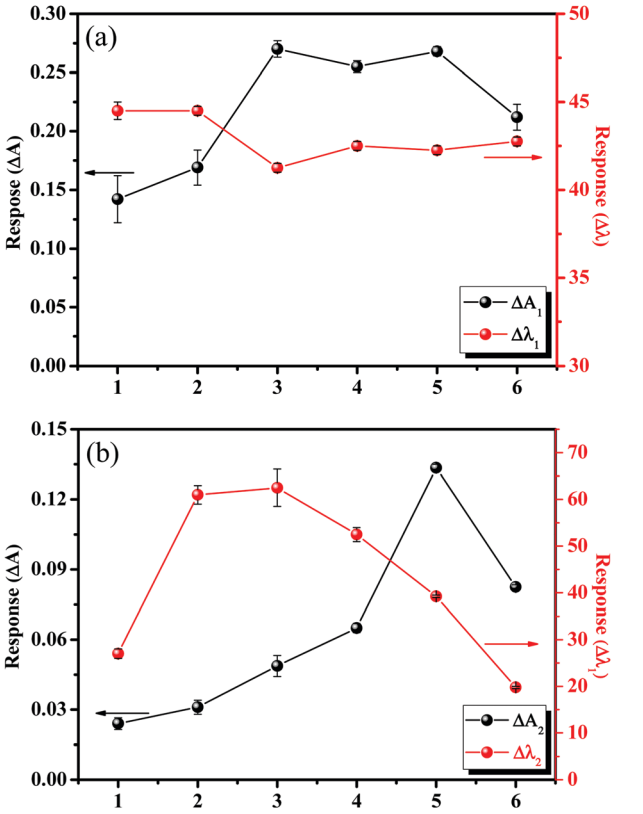


Fig. 4 RI responses (changing from air to water) of glass slides deposited with Au nano-urchins: (a) response of the first peak; (b) response of the second peak.

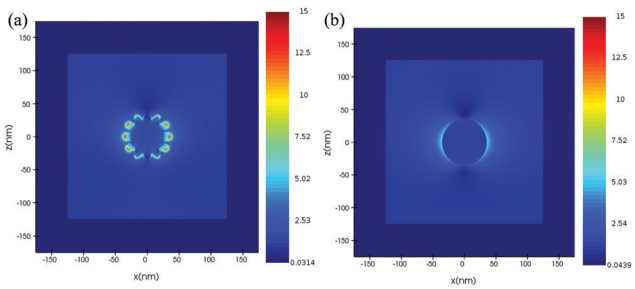


Fig. 5 Electromagnetic field amplitude patterns of (a) Au nano-urchin and (b) Au nano-sphere simulated using an FDTD solution. A local field enhancement contour plot of the Au nano-urchin and nano-sphere excited at 550 nm in air.

and second peak positions, and $A_1$ and $A_2$ were the absorbance values at $\lambda_1$ and $\lambda_2$, respectively. Slides 2, 3, and 4 had better response characteristics. The average values of $\Delta\lambda_2$ were 61 nm, 63 nm, and 52 nm for slides 2, 3, and 4, respectively. Most of the Au nano-urchins are monomers (glass slide 1), and the number of Au nano-urchin dimers and polymers increases on slide 2 to 6. However, big aggregates were found on slides 4, 5, and 6, and their RIS began to decrease, which was ascribed to the covering of effective RIS sensing regions in big Au nano-urchin aggregates.[41] Therefore, RIS enhancements were mainly attributed to electric field coupling effects among nano-urchins, especially dimers.

For further understanding the tip effect, FDTD simulations have been performed to resolve and compare the distribution of the electric field surrounding the simulated Au nano-urchin and nano-sphere (Fig. 5). The result showed that the strongest electric field region was located at the sharp tips (hot-spot). To further understand the electric field enhancement by coupling between Au nano-urchins, the simulated electric field was plotted as a function of the inter-particle spacing (Fig. 6). The electric field distribution of the single nano-urchin excited at 785 nm was weaker than that at 540 nm. With inter-particle distance decreasing from 50 to 1 nm, a much enhanced hot spot was generated in between when the inter-particle distance decreased to less than 5 nm, which could be used to explain the RIS enhancement of Au nano-urchins deposited on glass slides number 2 to 4.

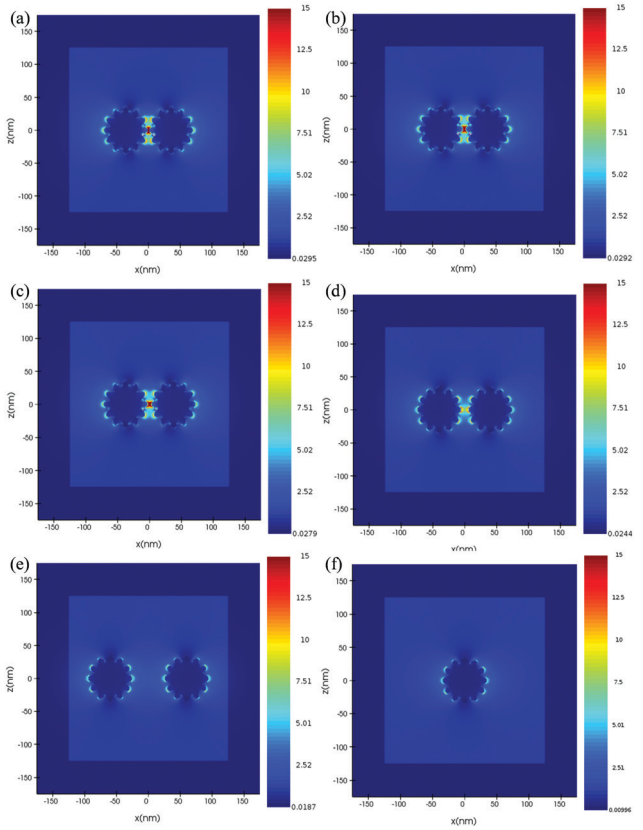


Fig. 6 Electromagnetic field amplitude patterns of a pair of Au nano-urchins 70 nm in diameter with different inter-particle gaps: (a to e) 1, 3, 5, 10, 50 nm; (f) a single Au nano-urchin simulated using an FDTD solution. The simulations were carried out for an excitation wavelength of 785 nm.

### 3.3 MISG@Au nano-urchin sensors and vapor sensing performance

Spin-coating was used to generate MISG layers on the Au nano-urchin slides (MISG@Au nano-urchin sensors). For glass slide number 2, Fig. S7(a) (ESI†), where the spin-coating speed changed from 1000 rpm to 5000 rpm, the second spectral peak disappeared (MISG solution: 18 μL). Glass slide number 4 had a stronger second peak and was coated with 18 μL of MISG at various spin-coating speeds, see Fig. S7(b) (ESI†); and the second peak red-shifted *versus* spin-coating speed. The pre-polymerization may have made the MISG solution viscous, which might have changed the original distribution of nano-urchins during spin-coating. Thereafter, the amount of MISG was decreased to 12 μL [Fig. S5(c), ESI†], 8 μL [Fig. S5(d), ESI†], and 4 μL [Fig. S5(e), ESI†]. When the amount of MISG solution decreased, the second peak blue-shifted. As a result, the slow spin-coating speed did not shift the second peak position. A comparison of the different amounts of MISG solution spin-coated at 1000 rpm is summarized in Fig. S5(f) (ESI†). The optimal conditions for making the MISG@Au nano-urchin sensor were spin-coating 6 μL of MISG at 1000 rpm for 1 min. These conditions might have had less of an effect on the distribution of nano-urchins. As shown in Fig. 7, nano-urchins were visible under the MISG layer; hence, the MISG thickness was

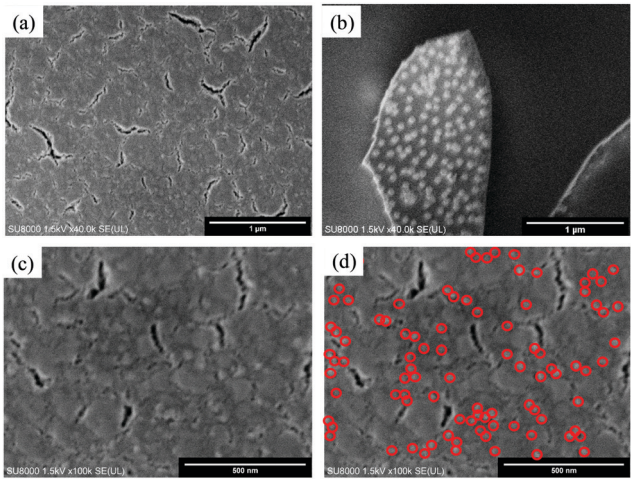


Fig. 7 SEM images of the optimized MISG@Au nano-urchin sensor (glass slide number 3, MISG: 6 μL, 1000 rpm for 1 min).

probably in the nanometer range. Lines drawn on the surface of MISG@Au nano-urchin sensors with a small pincer verified that the distribution of nano-urchins was nearly unaffected.

The MISG solution was spin-coated on Au nano-urchins deposited on slides numbered 2, 3, 4, and 5 to compare the responses to *cis*-jasmine vapor (gas flow rate: 0.5 L $min^{-1}$). The optical characteristics of the MISG@Au nano-urchin sensors on 2, 3, 4, and 5 are plotted in Fig. 8(a). All the spectra had two peaks, and the response of the sensors to *cis*-jasmine are compared in Fig. 8(b). Number 3 had the largest response, especially for the $\Delta\lambda_2$ parameter, which was twice that of $\Delta\lambda_1$. Therefore, the hot spot generated by the electric field coupling among the Au nano-urchins played a significant role in detecting the RI change.

The selectivity of the MISG-coated sensors for the *cis*-jasmine, α-pinene, limonene, and γ-terpinene targets was evaluated in terms of $R_{\text{normalized}}$, given by:

$$R_{\text{normalized}} = \frac{R}{\lg C_{\text{vapor}}} \quad (3)$$

where $R$ was the spectral response ($\Delta A_1$, $\Delta A_2$, $\Delta\lambda_1$ and $\Delta\lambda_2$) and $C_{\text{vapor}}$ was the concentration of the terpene vapor. As shown in Fig. 9, the largest sensor responses were for the corresponding imprinted terpene templates. According to the Finite-Difference Time-Domain (FDTD) simulations of J. F. Masson *et al.* and simulations in this work,[42] the electric-field enhancement occurred at sharp branched tips, and the electric-field coupling between the branches was much stronger than that between the nano-spheres. Hence, it was likely that there were many electric-field hot spots in the MISG@Au nano-urchins, because of their branched structures and the electric-field coupling among the Au nano-urchins. The latter was also responsible for the selectivity of the MISG@Au nano-urchin sensors.

To visualize clustering of the terpene samples in low dimensions, PCA was performed on the normalized responses ($M_{36\times16}$). The recognition patterns are shown in Fig. 10 for the four terpenes; each sensor had sixteen parameters: $\Delta A_1$, $\Delta\lambda_1$,

 

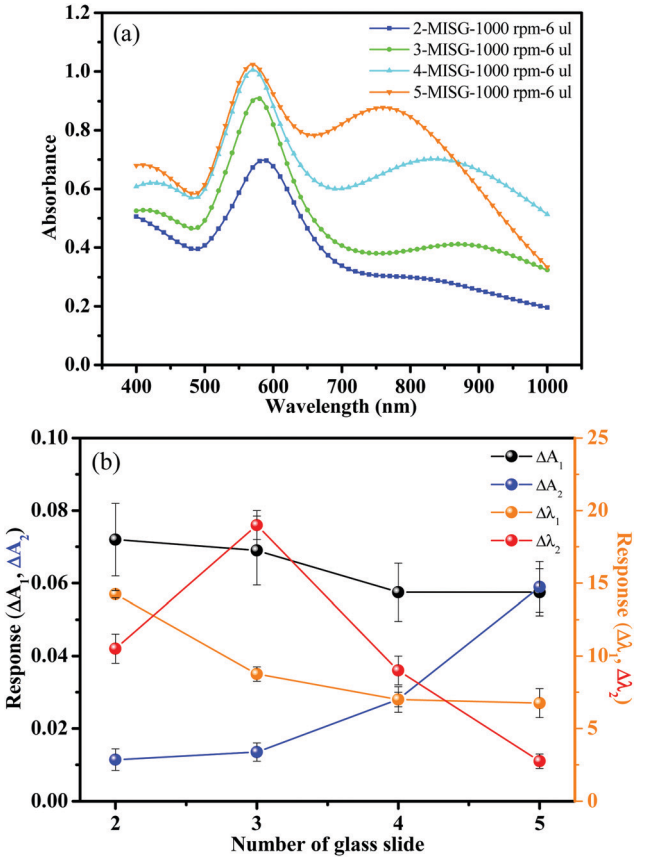


Fig. 8 (a) Spectra of MISG-coated glass slides with different densities of deposited Au nano-urchins (1000 rpm, 6 μL of MISG); (b) $R_{normalized}$ for $MISG_{jas}$-coated Au nano-urchin sensor to *cis*-jasmine vapor.

$\Delta A_2$, and $\Delta\lambda_2$ for $MISG_{jas}$, $MISG_{lim}$, $MISG_{pin}$, and $MISG_{ter}$. For each vapor, three gas flow rates (0.3 L $min^{-1}$, 0.5 L $min^{-1}$, and 0.7 L $min^{-1}$) were measured and repeated three times. Hence, a data set of 36 samples (4 VOCs × 3 gas flow rate × 3 repeats) was collected for the PCA analysis. Because PCA is unsupervised, the samples were clustered together based on similarities and differences in their principal component (PC) scores. The original variables used to perform the PCA are summarized in Table S1 (ESI†), and the PC1, PC2, and PC3 loadings are listed in Table S2 (ESI†). The first three PCs that possessed 88.86% of the cumulative variance proportion of the response data are plotted in Fig. 10, where each of the four vapors occupied separate regions in the PC space. In Table S2 (ESI†), larger loadings of PC 1, 2, and 3 were obtained both from the spectral responses of the first spectral peaks ($\Delta A_1$ and $\Delta\lambda_1$) and the second spectral peaks ($\Delta A_2$ and $\Delta\lambda_2$), which verified that both peaks were necessary for terpene discrimination and classification. In PC3, the four vapors could be sorted by their vapor pressures in descending order (α-pinene > limonene > γ-terpinene > *cis*-jasmone), which indicated that vapor pressure information might have been contained in PC3. According to the loadings of PC3, the corresponding response parameter $\Delta\lambda_2$ had the largest contribution. Therefore, $\Delta\lambda_2$ might have had a large role in vapor pressure discrimination.

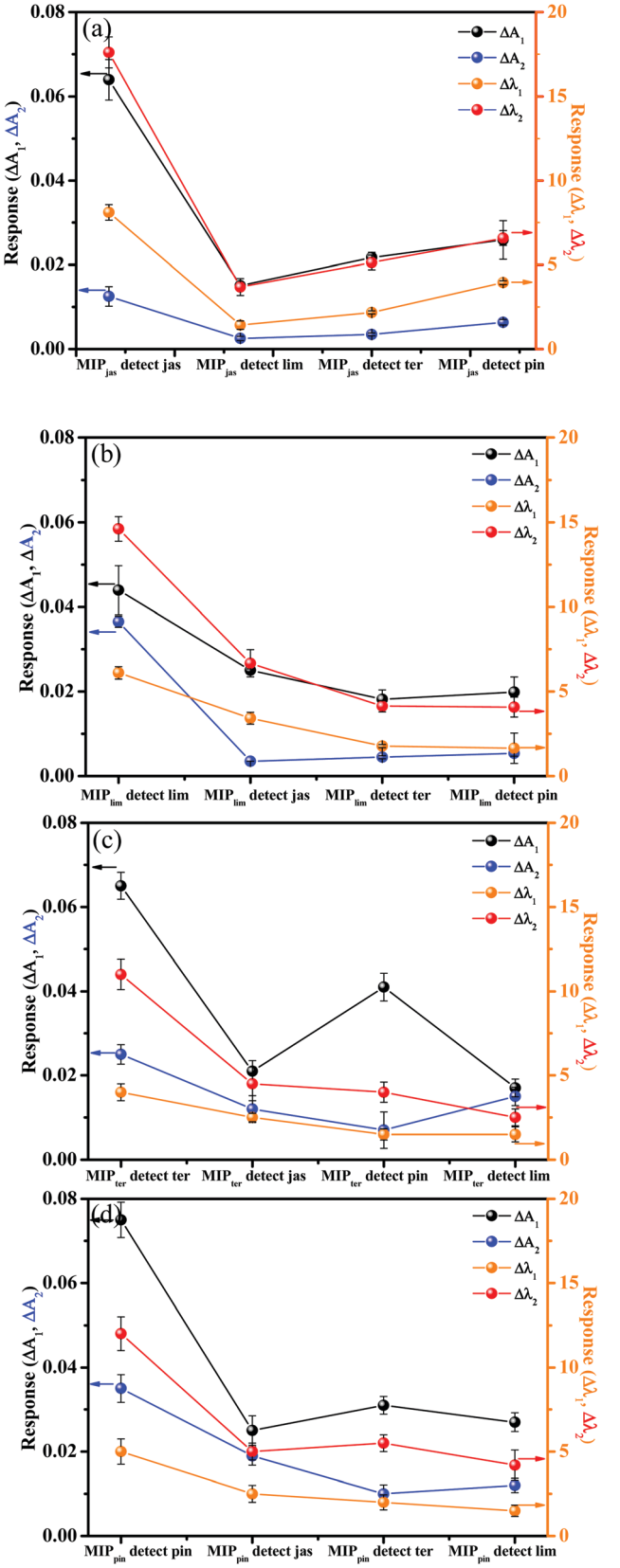


Fig. 9 $R_{normalized}$ for (a) $MISG_{jas}$, (b) $MISG_{ter}$, (c) $MISG_{lim}$, and (d) $MISG_{pin}$ to *cis*-jasmine, γ-terpene, limonene, and α-pinene vapors, respectively.

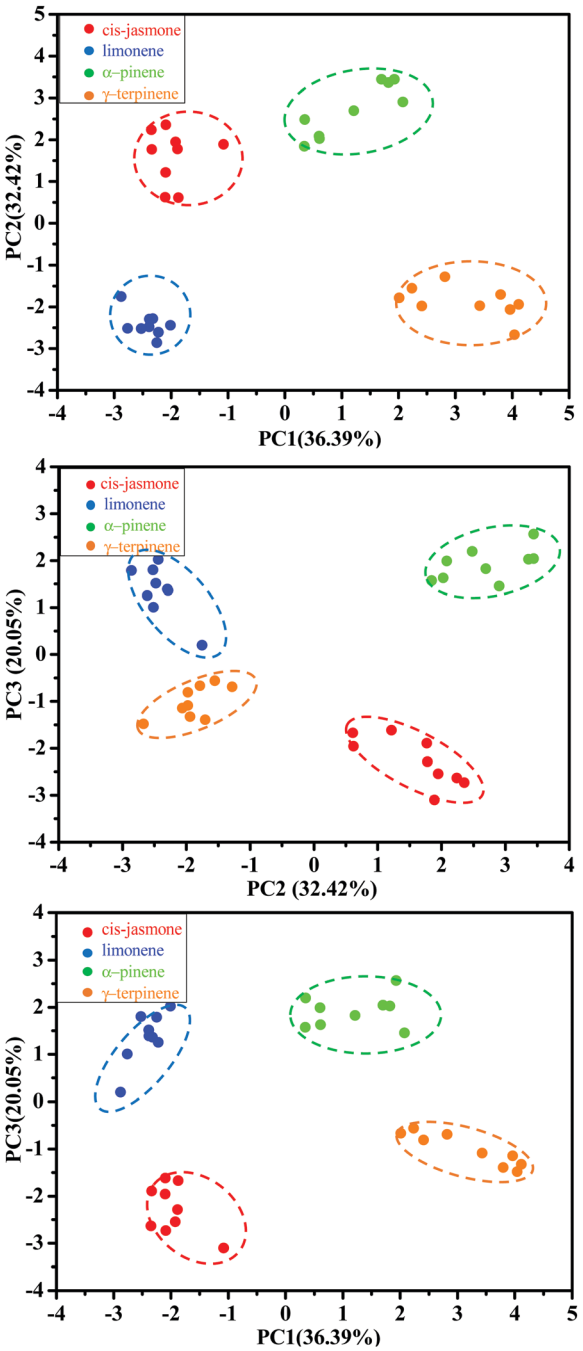


Fig. 10 PCA score plots of 36 sample responses to *cis*-jasmone, limonene, α-pinene, and γ-terpinene vapors.

## 4. Conclusions

Branched Au nano-urchins with a diameter of approximately 60 nm were synthesized and deposited with controllable densities on glass slides. The deposited Au nano-urchins exhibited two absorption peaks at 550 nm and 785 nm. By controlling the deposition density, the intensities of the two peaks were controlled. A MISG solution was spin-coated on the deposited Au nano-urchins with various amounts of MISG and spin-coating speeds. The combination of 6 μL of MISG solution with a spin-coating speed of 1000 rpm was found to be optimum because it had a negligible effect on the initial distribution of nano-urchins. Four MISGs were specifically developed for *cis*-jasmine, limonene, α-pinene, or γ-terpinene detection. The normalized responses of the MISG@Au nano-urchin sensors to the terpene vapors exhibited selectivity to the corresponding template molecules. The sensitivity was attributed to the electronic hot spots generated by Au nano-urchins and to the coupling among nano-urchins. The four terpene vapors were classified into four clusters using PCA, and the classification was dependent on both spectral peaks.

## Conflicts of interest

There are no conflicts to declare.

## Acknowledgements

This study was supported by the National Nature Science Foundation of China No. 61801400 and No. 61703348, JSPS KAKENHI Grant Number JP18F18392, and Central Universities under Grant number XDJK2018C021.

## Notes and references

1 T. J. A. Bruce and J. A. Pickett, *Phytochemistry*, 2011, **72**, 1605.
2 T. J. A. Bruce, *Front. Plant Sci.*, 2014, **5**, 349–351.
3 C. Calfapietra, S. Fares and F. Lofeto, *Environ. Pollut.*, 2009, **157**, 1478.
4 J. K. Holopainen and J. Gershenzon, *Trends Plant Sci.*, 2010, **15**, 176.
5 I. S. Sobhy, C. M. Woodcock, S. J. Powers, J. C. Caulfield, J. A. Pickett and M. A. Birkett, *J. Chem. Ecol.*, 2017, **43**, 39.
6 K. Kobayashi, *Environ. Microbiol.*, 2015, **17**, 1365.
7 J. S. Thaler, P. T. Humphrey and N. K. Whiteman, *Trends Plant Sci.*, 2012, **17**, 1360.
8 J. A. Pickett and Z. R. Khan, *New Phytol.*, 2016, **212**, 856.
9 Z. X. Han, M. M. Rana, G. F. Liu, M. J. Gao, D. X. Li, F. G. Wu, X. B. Li, X. C. Wan and S. Wei, *Food Chem.*, 2016, **212**, 739.
10 T. R. Duhl, D. Helmig and A. Guenther, *Biogeosciences*, 2008, **5**, 761.
11 M. Bruinsma, M. A. Posthumus, R. Mumm, M. J. Mueller, J. J. A. van Loon and M. Dicke, *J. Exp. Bot.*, 2009, **60**, 2575.
12 M. Garbuzov and F. L. W. Ratnieks, *Funct. Ecol.*, 2014, **28**, 364.
13 J. P. Graça, T. E. Ueda, T. Janegitz, S. S. Vieira, M. C. Salvador, M. C. N. Oliveira, S. M. Zingaretti, S. J. Powers, J. A. Pickett, M. A. Birkett and C. B. Hoffmann-Campo, *Phytochemistry*, 2016, **131**, 84.
14 M. Yu, X. Hou, Q. Liu, Y. Wang, J. Liu and G. Jiang, *Talanta*, 2017, **164**, 141.

 

15 G. C. Graffius, B. M. Jocher, D. Zewge, H. M. Halsey, G. Lee, F. Bernardoni, X. Bu, R. Hartman and E. L. Regalado, *J. Chromatogr. A*, 2017, **1518**, 70.
16 B. Bojko, F. Mirnaghi and J. Pawliszyn, *Bioanalysis*, 2011, **3**, 1895.
17 K. Arshak, E. Moore, G. M. Lyons, J. Harris and S. Clifford, *Sens. Rev.*, 2004, **24**, 181.
18 A. Bearzotti, A. Macagnano, P. Papa, I. Venditti and E. Zampetti, *Sens. Actuators, B*, 2017, **240**, 1160.
19 D. Zhang, J. Liu, C. Jiang, A. Liu and B. Xia, *Sens. Actuators, B*, 2017, **240**, 55.
20 M. T. Sun, H. Yu, H. J. Zhu, F. Ma, S. Zhang, D. J. Huang and S. H. Wang, *Anal. Chem.*, 2014, **86**, 671.
21 K. M. Mayer and J. H. Hafner, *Chem. Rev.*, 2011, **111**, 3828.
22 S. Szunerits and R. Boukherroub, *Chem. Commun.*, 2012, **48**, 8999.
23 A. Amirjani and D. H. Fatmehsari, *Talanta*, 2018, **176**, 242.
24 A. Danilov, G. Tselikov, F. Wu, V. G. Kravets, I. Ozerov, F. Bedu, A. N. Grigorenko and A. V. Kabashin, *Biosens. Bioelectron.*, 2018, **104**, 102.
25 D. Hao, C. Hu, J. Grant, A. Glidle and D. R. S. Cumming, *Biosens. Bioelectron.*, 2018, **100**, 23.
26 M. Lu, H. Zhu, C. G. Bazuin, W. Peng and J. F. Masson, *ACS Sens.*, 2019, **4**, 613.
27 B. Chen, C. Liu, L. Ge and K. Hayashi, *Sens. Actuators, B*, 2016, **231**, 787.
28 L. Shang, C. Liu, B. Chen and K. Hayashi, *Sens. Actuators, B*, 2018, **260**, 617.
29 A. Feinle, M. S. Elsaesser and N. Hüsing, *Chem. Soc. Rev.*, 2016, **45**, 3377.
30 U. Latif, A. Rohrer, P. A. Lieberzeit and F. L. Dickert, *Anal. Bioanal. Chem.*, 2011, **400**, 2457.
31 Z. Nenova, S. Kozhukharov, T. Nenov, N. Nedev and M. Machkova, *Sens. Actuators, B*, 2016, **224**, 143.
32 L. Shang, C. Liu, B. Chen and K. Hayashi, *ACS Sens.*, 2018, **3**, 1531.
33 S. P. Kumar, *Nanotechnology*, 2008, **19**, 015606.
34 J. Li, J. Wu, X. Zhang, Y. Liu, D. Zhou, H. Sun, H. Zhang and B. Yang, *J. Phys. Chem. C*, 2011, **115**, 3630.
35 L. Chen, Y. Huang, T. T. Xing, L. Ge, T. Yang, B. Chen and C. Z. Huang, *J. Mater. Chem. C*, 2017, **5**, 7806.
36 L. Shang, C. Liu, M. Watanabe, B. Chen and K. Hayashi, *Sens. Actuators, B*, 2017, **249**, 14.
37 J. Qiu and W. D. Wei, *J. Phys. Chem. C*, 2014, **118**, 20735.
38 P. K. Jain, W. Huang and M. A. El-Sayed, *Nano Lett.*, 2007, **7**, 2080.
39 I. Blakey, Z. Merican and K. J. Thurecht, *Langmuir*, 2013, **29**, 8266.
40 K. Saha, S. S. Agasti, C. Kim, X. Li and V. M. Rotello, *Chem. Rev.*, 2012, **112**, 2739.
41 J. Ye, K. Bonroy, D. Nelis, F. Frederix, J. D'Haenc, G. Maes and G. Borghs, *Colloids Surf., A*, 2008, **321**, 313.
42 H. Yockell-Lelièvre, F. Lussier and J. F. Masson, *J. Phys. Chem. C*, 2015, **119**, 28577.